Supplemental Information

High-Performance All-small-molecule Organic Solar Cells without Interlayers

Rui Sun[1], Yao Wu[1], Jie Guo[1], Yuheng Wang[4], Fei Qin[5], Bingxiu Shen[6], Donghui Li[7],

Tao Wang[7], Yaowen Li[6], Yinhua Zhou[5], Guanghao Lu[4], Yongfang Li[2], Jie Min[1,2,3]*

[1]The Institute for Advanced Studies, Wuhan University, Wuhan 430072, China
E-mail: min.jie@whu.edu.cn

[2]Beijing National Laboratory for Molecular Sciences, Beijing 100190, China

[3]Key Laboratory of Materials Processing and Mold (Zhengzhou University), Ministry of Education, Zhengzhou, 450002 China

[4]Frontier Institute of Science and Technology, Xi'an Jiaotong University, Xi An 710054, China

[5]Wuhan National Laboratory for Optoelectronics and School of Optical and Electronic Information, Huazhong University of Science and Technology, Wuhan 430074, China

[6]Laboratory of Advanced Optoelectronic Materials College of Chemistry Chemical Engineering and Materials Science, Soochow University, Suzhou 215123, China

[7]State Key Laboratory of Silicate Materials for Architectures, Wuhan University of Technology, Wuhan 430070, China

1. Experimental Section

1.1. Materials

Materials: Yao Wu synthesized the Y6 material. B1, BTP-eC9, BTR-Cl, and PFN-Br were purchased from Solarmer Materials Inc, and Yao Wu conducted further purification for B1, BTP-eC9, and BTR-Cl materials. Solvents (chloroform and chlorobenzene) were dried and distilled from appropriate drying agents prior to use. The processes of the purification of solvents are as followed: The purifications involve washing with water for several times to remove the ethanol, drying with potassium carbonate, refluxing with calcium chloride, and then distilling. The distilled CF and CB were stored in the dark to avoid the photochemical formation of phosgene.

1.2. Device Fabrication and Testing

Control solar cell devices fabrication: The control solar cell devices were fabricated with a conventional structure of Glass/ITO/PEDOT: PSS(40 nm)/Active layer (donor: acceptor (D: A) for bulk heterojunction (BHJ) blend)/PFN-Br(5nm)/Al. Pre-patterned ITO coated glass substrates (purchased from Advanced Election Technology Co., Ltd, the sheet resistance of the ITO glass was about 7-9 Ω) washed with methylbenzene, deionized water, acetone, and isopropyl alcohol in an ultrasonic bath for 15 minutes each. After blow-drying by high-purity nitrogen, all ITO substrates are cleaned in the ultraviolet ozone cleaning system for 15 minutes. Subsequently, a thin layer of PEDOT: PSS (Xi'an Polymer Light Technology Corp 4083) was deposited through spin-coating on pre‑cleaned ITO-coated glass at 4000 rpm for 30 s and dried subsequently at 150 °C for 15 minutes in atmospheric air. Then the photovoltaic layers were spin-coated in a glovebox from a solution of B1:BTP-eC9 (1.6:1, w/w) with 18 mg mL^{-1} in chloroform. A PFN-Br layer via a solution concentration of 0.5 mg mL^{-1} was deposited at the top of the active layer at a rate of 4000 rpm for 30 s. Finally, the top aluminum electrode of 100 nm thickness was thermally evaporated through a mask onto the cathode buffer layer under a vacuum of ～5×10^{-6} mbar. The optimal active layer was fabricated by

spin-coating at 2000rpm for the 30s and then thermal annealing at 140 $^{\circ}$C for 2 minutes. The thickness optimal active layer measured by a Bruker Dektak XT stylus profilometer was about 110 nm. The typical active area of the investigated devices was 5 mm^2.

Metal-Semiconductor layer -Metal (MSM)-type solar cell devices fabrication: The metal-semiconductor layer -metal (MSM)-type solar cell devices were fabricated with the structure of Glass/ITO-Cl/Active layer (donor: acceptor (D:A) for bulk heterojunction (BHJ) blend)/Al. Pre-patterned ITO coated glass substrates (purchased from Advanced Election Technology Co., Ltd, the sheet resistance of the ITO glass was about 7-9 Ω) washed with methylbenzene, deionized water, acetone, and isopropyl alcohol in an ultrasonic bath for 15 min each. After blow-drying by high-purity nitrogen, all ITO substrates are cleaned in the ultraviolet ozone cleaning system for 15 minutes. All the cleaned ITO glass is next placed in the UV-Ozone cleaning instrument using ultraviolet ozone light irradiation for 15 min to obtain the UV-Ozone treated ITO anode. Afterward, the ITO surface was covered with 1ml chlorobenzene (Sigma-Aldrich) in a Pyrex Petri dish under UV treatment for 0-20 min. After cleaning the surface of ITO glass, UV-ozone treatment is applied for 15 min to obtain the surface chlorinated ITO anode. Then the photovoltaic layers were spin-coated in a glovebox from a solution of B1:BTP-eC9 (1.6:1, w/w) with 18 mg mL^{-1} in chloroform. The methanol solution was deposited at the top of the active layer at a rate of 4000 rpm for 30 s. Finally, the top aluminum electrode of 100 nm thickness was thermally evaporated through a mask onto the cathode buffer layer under a vacuum of ～5×10^{-6} mbar. The optimal active layer was fabricated by spin-coating at 1500rpm for the 30s and then thermal annealing at 140 $^{\circ}$C for 2 min. The thickness optimal active layer measured by a Bruker Dektak XT stylus profilometer was about 110 nm. The typical active area of the investigated devices was 5 mm^2.

The current-voltage characteristics of the solar cells were measured by a Keithley 2400 source meter unit under AM1.5G (100 mW cm^{-2}) irradiation from a solar simulator (Enlitech model SS-F5-3A). Solar simulator illumination intensity was determined at 100 mW cm^{-2} using a monocrystalline silicon reference cell with a KG5 filter. Short circuit currents under AM1.5G (100 mW cm^{-2}) conditions were estimated from the

spectral response and convolution with the solar spectrum. The external quantum efficiency was measured by a Solar Cell Spectral Response Measurement System QE-R3011(Enli Technology Co., Ltd.).

1.3 Instruments and Characterization

Optical measurements and simulations: Ultraviolet-visible near-infrared (UV-vis-NIR) absorption spectra were recorded with a Perkin-Elmer Lambda 365 UV-Vis spectrophotometer from 300 nm to 1100 nm. The optical simulations were calculated by Fluxim Setfos software.

Work function measurements: Work function of samples were measured using scanning Kelvin probe (KP020, KP technology). Highly oriented pyrolytic graphite (HOPG) with a work function of 4.5 eV is used as a reference sample.

X-ray photoelectron spectroscopy (XPS) measurements: This experiment uses an X-ray photoelectron spectrometer (ThermoFischer, ESCALAB Xi+, USA) for testing. Among them, the vacuum degree of the analysis chamber is $8*10^{-10}$ Pa, the excitation source is Alka rays (hv=1486.6eV), the working voltage is 12.5 kV, the filament current is 16 mA, and the signal accumulation is performed for 10 cycles. Test Passing-Energy full-spectrum is 100ev, the narrow spectrum is 20eV, step length is 0.05eV, the residence time is 40-50ms, and C1s=284.80eV binding energy is used as the energy standard for charging correction.

Ultraviolet Photoelectron Spectrometer (UPS) measurements: UPS spectra were measured with Thermo K-Alpha$^+$ and used the HeI (21.22eV) emission line.

Atomic force microscopy (AFM) measurements: AFM measurements were performed by using a Nano Wizard 4 atomic force microscopy (JPK Inc. Germany) in Qi mode to observe the films surface morphologies of the ITO/PEDOT:PSS/Active layer, ITO/PEDOT:PSS/active layer/Methanol, ITO-Cl/Active layer and ITO-Cl/Active layer/Methanol.

Kelvin Probe Force Microscopy measurements: The frequency-modulation (FM)

SKPM was operated combined with a Cypher S AFM (Asylum Research, Oxford Instruments) and a HF2LI Lock-in amplifier (Zurich Instruments). The resonance frequency $\omega 0$ and spring constant of AFM conducting tips are around 140kHz and $5.0Nm^{-1}$, respectively.

FIB-TEM measurements: The lift-out sample for TEM was prepared using an FEI Helios Nanolab 660 DualBeam FIB from the area-of-interest containing all layers of the solar cell. A lamella containing a cross-section of the solar cell was then attached to a TEM half-grid for final thinning. TEM was performed on an FEI TITAN3 Themis 60–300 double aberration-corrected microscope at the Shenzhen Cauchy Data Co. Ltd, equipped with a Super-X energy dispersive spectrometer.

Film-depth-dependent light absorption spectra measurements. Film-depth-dependent light absorption spectroscopy was conducted by a home-made setup. Low-pressure (less than 20 Pa) oxygen plasma was used for the incremental etching of the film. The UV–Vis absorption spectrum after each etching was monitored by an optical spectrometer. Beer-Lambert's law was utilized to fit the film-depth-dependent light absorption spectra. The detailed methods about the measurements and numerical fitting were available elsewhere[1].

Space charge limited current (SCLC) measurements: Single carrier devices were fabricated, and the dark current-voltage characteristics measured and analyzed in the space charge limited (SCL) regime. The structure of hole-only control devices was Glass/ITO/PEDOT: PSS/Semiconductor layer/MoOx (10 nm)/Ag (100 nm) and Glass/ITO-Cl/Semiconductor layer/MoOx (10 nm)/Ag (100 nm) for MSM devices. The reported mobility data are average values over the six devices of each sample.

Photo-induced charge carrier extraction by linearly increasing the voltage (photo-CELIV) measurements: In photo-CELIV measurements, the devices were illuminated with a 405 nm laser diode. Current transients were recorded across the internal 50 Ω resistor of our oscilloscope. Here, a fast electrical switch was used to isolate the device

in order to prevent carrier extraction or sweep out. After the variable delay time, the switch connected the device to a function generator. It applied a linear extraction ramp, which was 40 μs long and 2.0 V high. Moreover, it started with an offset matching the V_{oc} of the device for each delay time. To determine the mobility in devices, photo-CELIV curves were measured using different experimental conditions, differing in delay time and applied voltage.

Transient photocurrent (TPC) measurements: Relevant control and MSM solar cells were excited with a 405 nm laser diode. The transient photocurrent response of the devices at short circuit conditions to a 200 μs square pulse from the LED with no background illumination. The current traces were recorded on a Tektronix DPO3034 digital oscilloscope by measuring the voltage drop over a 5-ohm sensor resistor in series with the solar cell. DC voltage was applied to the solar cell with an MRF544 bipolar junction transistor in a standard collector amplifier configuration.

Photoluminescence (PL)measurements: The PL data and emission of relevant films were collected using a Zolix Flex One Spectrometer. The PL excitation wavelength was set to 639 nm.
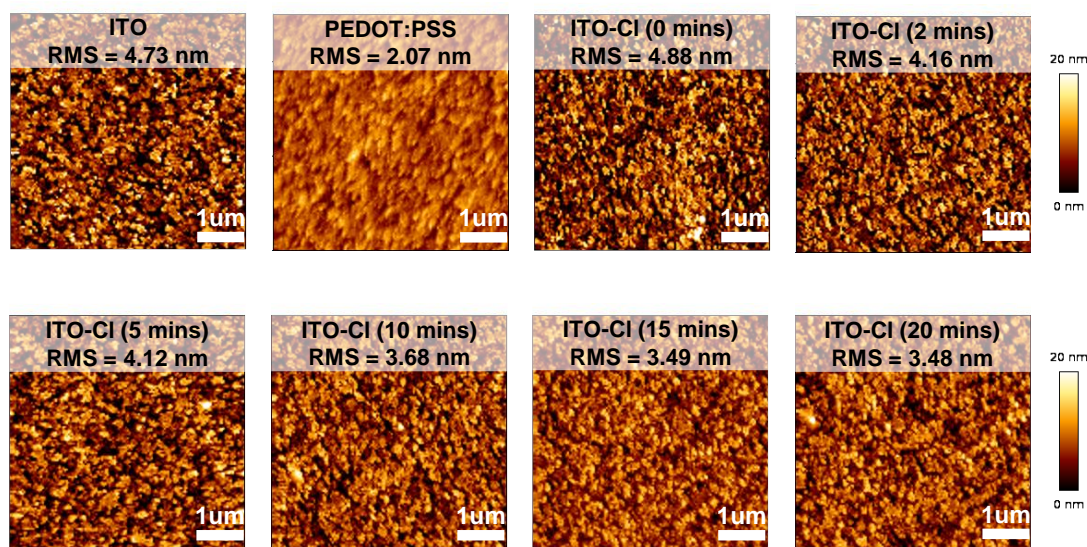
2. Figures and Tables

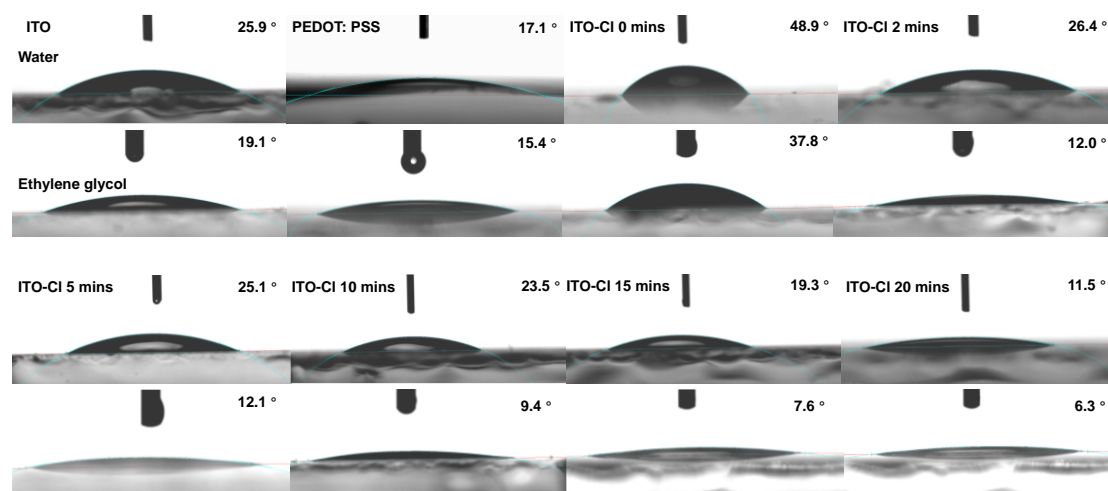**Figure S1**. 5 µm × 5 µm AFM topography images of ITO without and with surface chlorination treatment as a function of UV irradiation time, and the AFM top image of PEDOT:PSS layer coated on ITO substrate, respectively.

Figure S2. (a) Photographs of water and ethylene glycol droplets on the top surfaces of PEDOT:PSS layer and ITO anodes without and with surface chlorination treatment, as well as the respective contact angle values. The contact angle measurement is conducted at the center of the substrates, avoiding the edges of the ITO anodes.

Table S1. Investigations of the surface energy values of PEDOT:PSS layer and ITO anodes without and with surface chlorination treatment as a function of UV time.

Time (mins)	ITO	PEDOT : PSS	ITO-Cl 0 mins	ITO-Cl 2 mins	ITO-Cl 5 mins	ITO-Cl 10 mins	ITO-Cl 15 mins	ITO-Cl 20 mins
Surface Energy (mJ m^{-2})	104.5	119.84	64.47	96.41	99.53	101.38	109.2	121.44
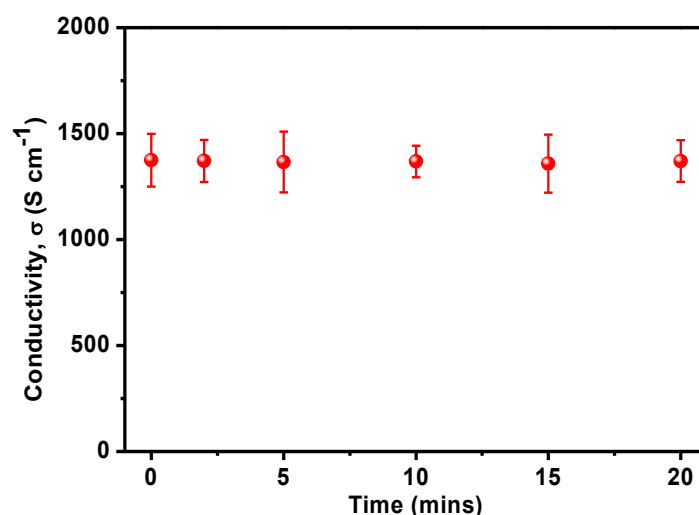
Figure S3. The electrical conductivity of the corresponding ITO electrodes as a function of surface chlorination treatment time from 0 to 20 min. The parallel electrical conductivities of relevant ITO anodes were measured using a lateral diode structure with two parallel Au electrodes.
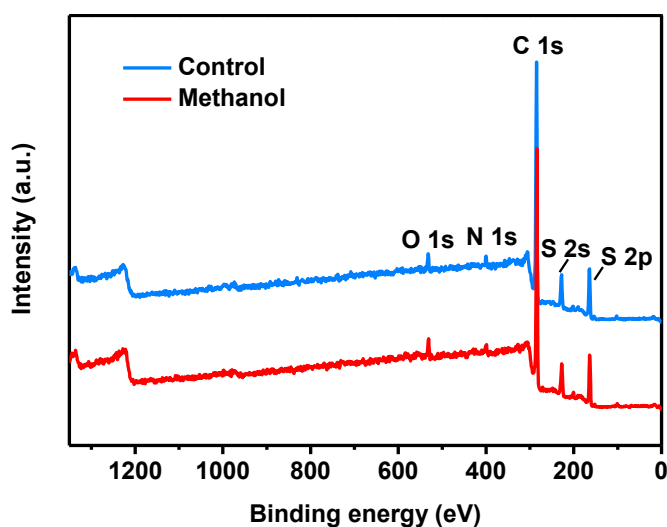
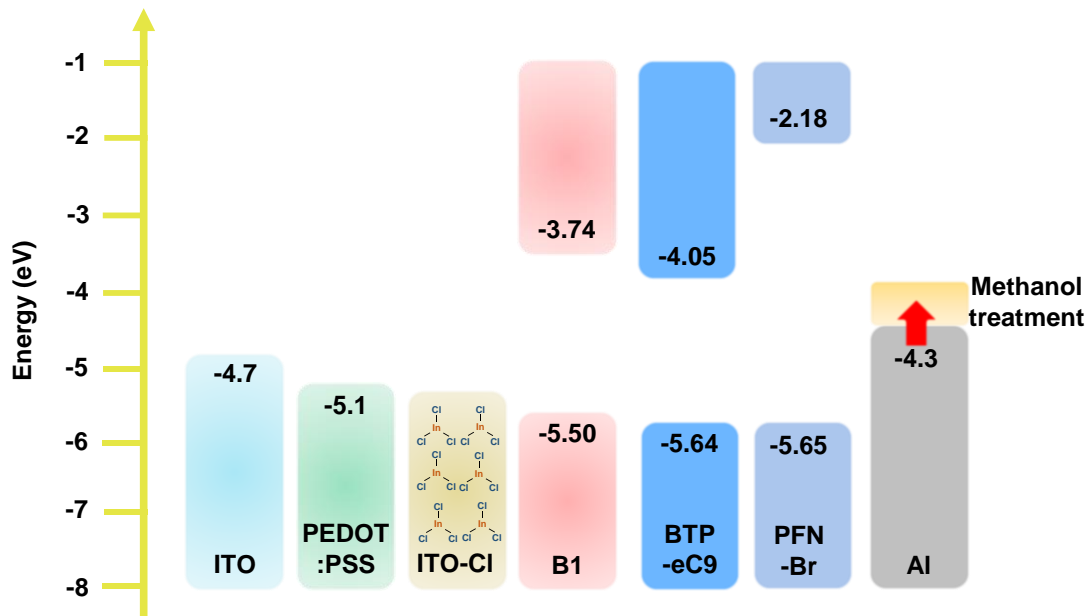**Figure S4**. XPS spectra of B1:BTP-eC9 blends without and with methanol treatment.

1

Figure S5. Energy level diagram of relevant OSCs. The commonly used electrodes in OSCs (typically indium tin oxide (ITO) with a low work function of ~4.7 eV and aluminum (Al) with a work function of ~4.3 eV) do not develop strong internal built-in filed (E_{in}) values, originating from the work function (or Fermi level (E_F)) difference between two electrodes in a control device structure. Using a combined surface chlorination and methanol treatment strategy, the WFs of anode and cathode can be modified effectively.
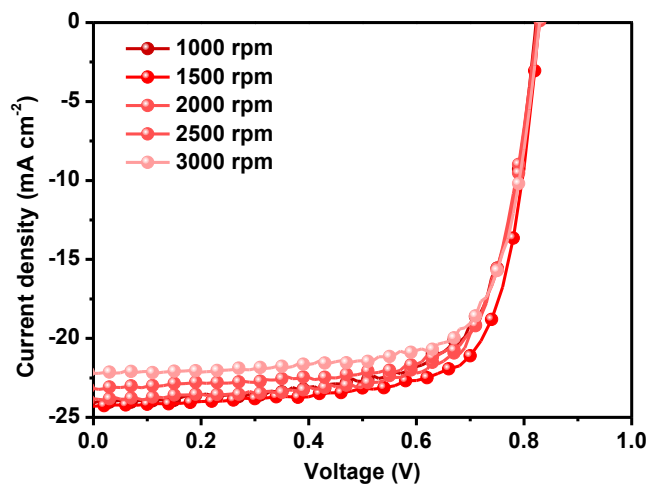

Figure S6. *J-V* curves of the devices based on B1:BTP-eC9 systems with different thickness, measured under the illumination of AM 1.5G at 100 mW cm^{-2}.

Table S2. Photovoltaic parameters of the devices based on B1:BTP-eC9 systems with different thickness, measured under the illumination of AM 1.5G at 100mW cm⁻².

| Active layer	Speed [rpm]	Thickness [nm]	V_{oc} [V]	J_{sc} [mA cm⁻²]	FF [%]	PCE [%]
	1000	119	0.822	24.08	69.45	13.76 (13.38)
	1500	110	0.827	24.30	73.92	14.86 (14.62)
B1:BTP-eC9	2000	100	0.825	23.82	72.60	14.27 (14.01)
	2500	82	0.829	23.16	72.63	13.94 (13.60)
	3000	74	0.827	22.20	73.23	13.44 (13.06)
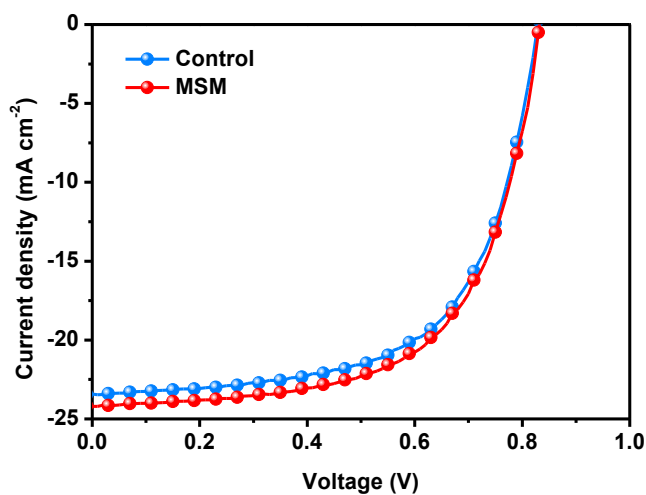
Figure S7. *J-V* curve characteristics of the control and MSM large area devices (1 cm²) based on the B1:BTP-eC9 system, measured under the illumination of AM 1.5G at 100 mW cm⁻².
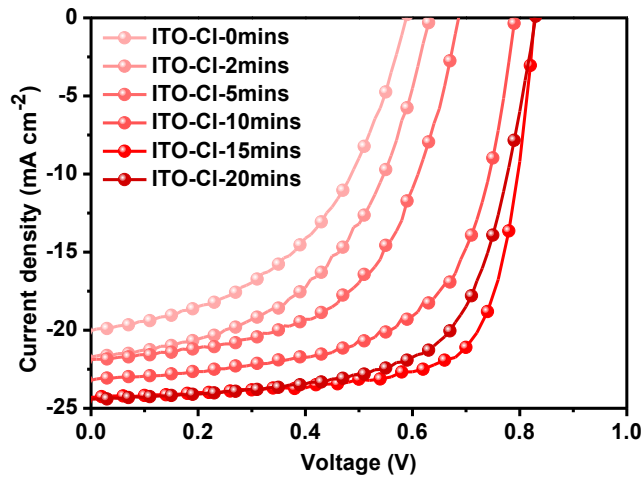
1
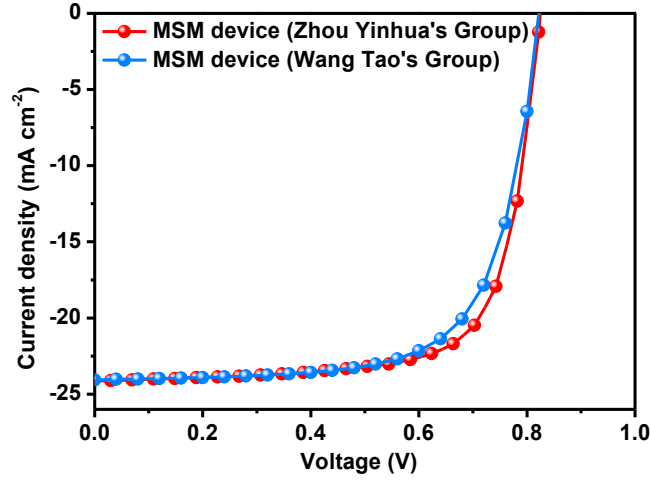
Figure S8. *J-V* curve characteristics of the MSM devices fabricated in Zhou Yinhua's group and Wang Tao's group based on the B1:BTP-eC9 system, measured under the illumination of AM 1.5G at 100 mW cm^{-2}.

5

6

Figure S9. *J-V* curve characteristics of the B1:BTP-eC9 devices with different UV treatment periods, measured under the illumination of AM 1.5G at 100 mW cm^{-2}.

9

10

11

12

13

14

15

Table S3. Photovoltaic parameters of the B1:BTP-eC9 devices with different UV treatment periods, measured under the illumination of AM 1.5G at 100 mW cm^{-2}. The values in parenthesis are the average PCEs obtained from 8 devices.

| Time [mins]	V_{oc} [V]	J_{sc} [mA cm^{-2}]	FF [%]	PCE [%]
0	0.588	20.02	56.11	6.61 (6.34)
2	0.631	21.71	57.77	7.91 (7.60)
5	0.685	21.89	61.61	9.24 (9.02)
10	0.791	23.19	64.95	11.91 (11.80)
15	0.827	24.30	73.92	14.86 (14.62)
20	0.830	24.41	67.11	13.60 (13.40)
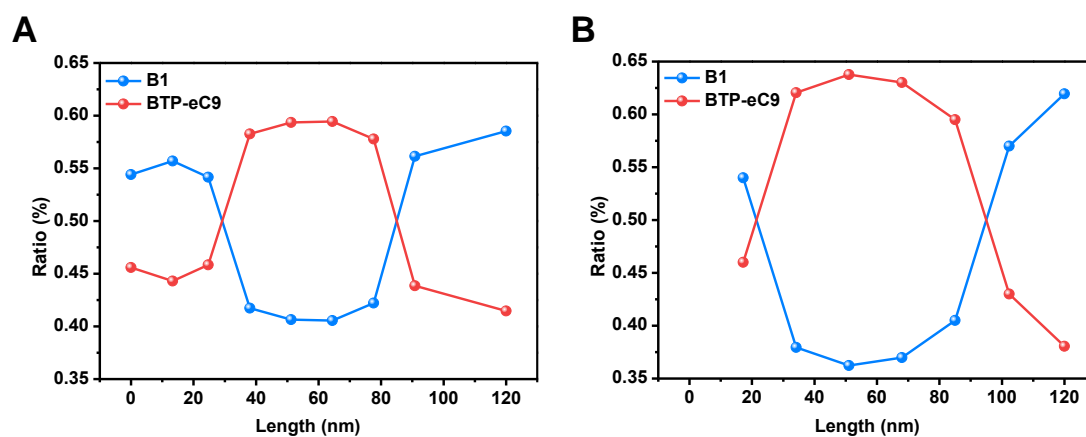
Figure S10. The vertical profiles of each component across the whole thickness of the active layers (A) in the control sample and (B) in the MSM sample, measured by in situ film-depth-dependent light absorption spectroscopy (FLAS) technique.
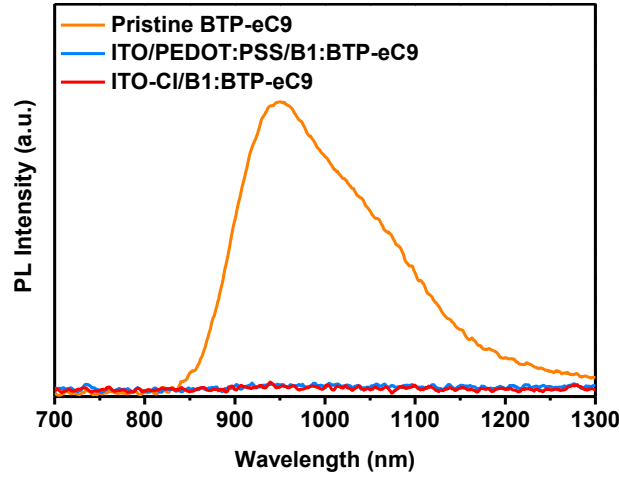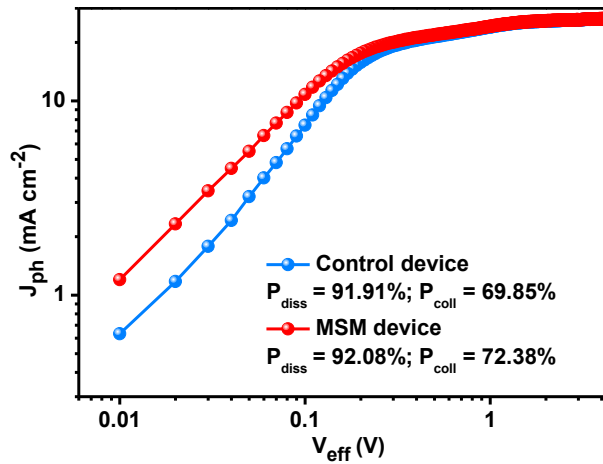
Figure S11. Photoluminescence (PL) spectra of neat acceptor Y6 film, and the active layers coated on ITO/PEODT:PSS and ITO-Cl substrates. Comparative studies of PL quenching (PLQ) efficiency shows that ITO-Cl/AL sample (92.27%) is slightly more efficient PL quencher than the ITO/PEODT:PSS/AL sample with a PLQ of 90.67%.


Figure S12. Photocurrent density (J_{ph}) *versus* effective bias (V_{eff}) characteristics based on optimized control and MSM devices. The difference on exciton dissociation and charge collection were gained by photocurrent density (J_{ph}) and the effective (V_{eff}) of the control and MSM devices. As depicted in fig. S9, photocurrent density (J_{ph}) versus effective voltage (V_{eff}) characteristics for the optimal control and MSM devices. J_{ph} is defined as $J_{ph} = J_L - J_D$ where J_L and J_D are the current densities under one sun illumination and in the dark, respectively. The V_{eff} is given by $V_{eff} = V_o - V$ where V_o is the voltage at which J_{ph} is 0 and V is the applied voltage. $P_{(E,T)} = J_{ph}/J_{sat}$ reflect the exciton dissociation and charge collection efficiency, where J_{sat} represents the saturation photocurrent density. When the $V_{eff} \gg 2.0V$, J_{sat} of the MSM-based solar cell is 25.84 mA cm^{-2}, which is higher than that of the control solar cell (J_{sat}= 25.72 mA cm^{-2}). This result mainly caused by the larger absorptivity to harvest more light in MSM devices. For the short-circuit conditions, $P_{(E,T)}$ is 91.91% for the control device,

and the value for the MSM device is 92.08%. The larger value of J_{ph}/J_{sat} for the MSM device implies the better charge extraction and collection, which contributes to the higher J_{sc} value.
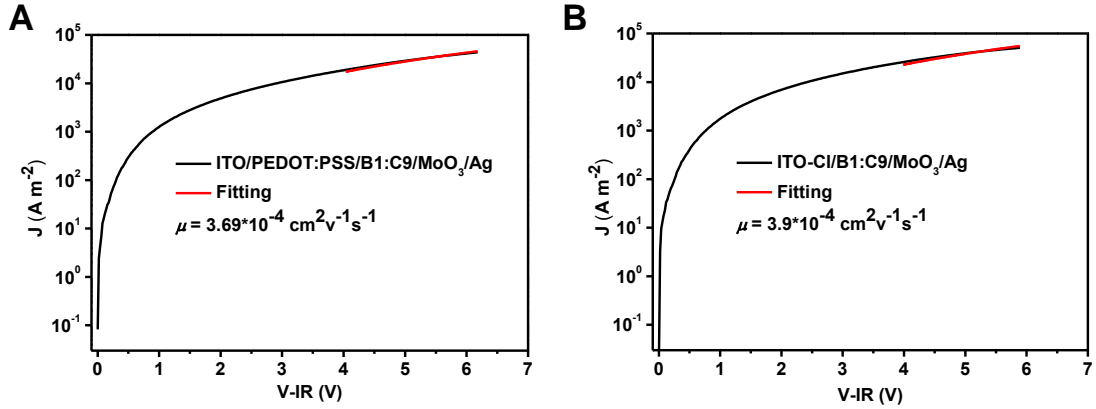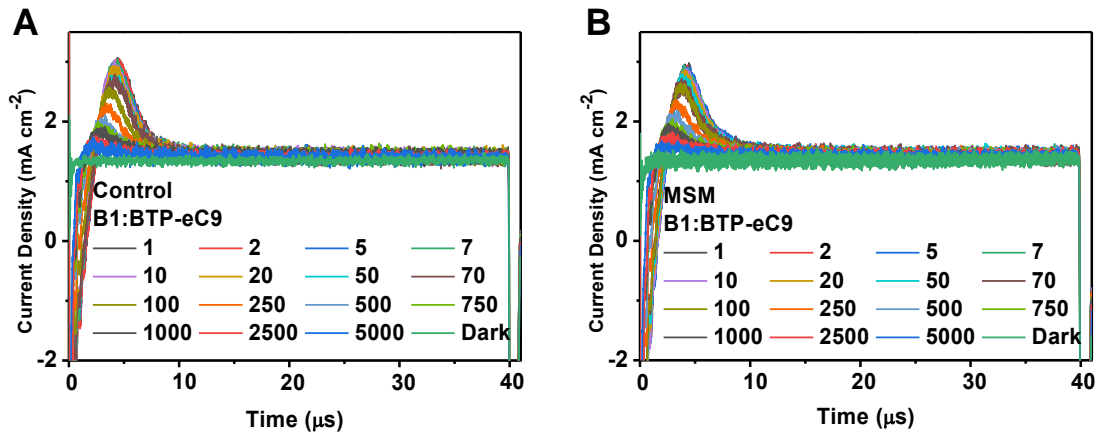

Figure S13. The dark J-V characteristics of control and MSM-type based hole-only devices. The solid lines represent the best fitting using the SCLC modified Mott-Gurney model.


Figure S14. Photo-CELIV measurements on the optimized (A) control and (B) MSM devices for different delay times between the light pulse and the extraction voltage ramp. To determine the mobility, fifteen photo-CELIV curves have been recorded using different experimental conditions for each sample. As shown in Fig. S10, photo-CELIV measurements carried out on control blend and MSM blend devices, photocurrent transients recorded by applying a 2V/40 µs linearly increasing reverse bias pulse after a 1 µs delay time. A very sharp peak is observed in the MSM devices indicated that charge extraction faster for MSM devices as compared to control devices. By changing the delay time and applied voltage to measuring the maximum charge extraction current (characterized by t_{max}), which occurs at maximum photocurrent.
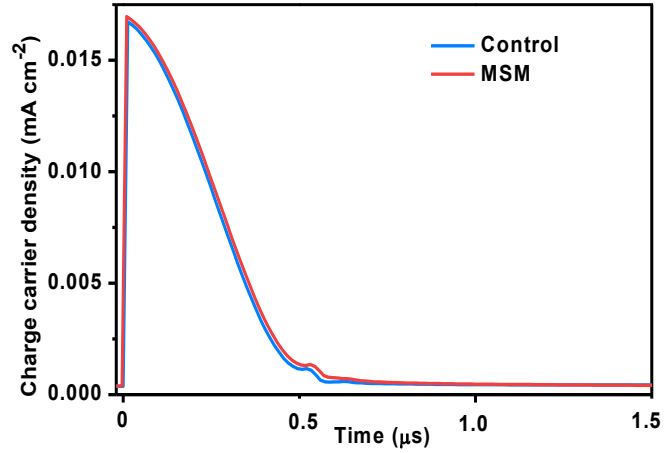
Figure S15. Charge extraction measurements of the control and MSM devices, measured under V_{oc} condition (one sun illumination). The carrier density could be increased by a reduction in the recombination rate in the MSM devices, measured under one sun illumination.

Table S4. Parameters extracted from photo-CELIV signals and SCLC and CE measurements based on the control and MSM devices under different conditions.

Device structures	μ_h[a] $[cm^2V^{-1}s^{-1}]$	μ[b] $[cm^2V^{-1}s^{-1}]$	n[c] $[cm^{-3}]$
Control	3.69×10^{-4}	5.24×10^{-5}	3.49×10^{16}
MSM	3.90×10^{-4}	5.84×10^{-5}	3.62×10^{16}

[a]For the SCLC measurements, the values were obtained based on six devices of each type, and the error bars represent plus or minus 1 standard deviation from the mean values (SCLC mobility). [b]The values were calculated from the Photo-CELIV measurements. [c]The values were measured by the CE measurements.
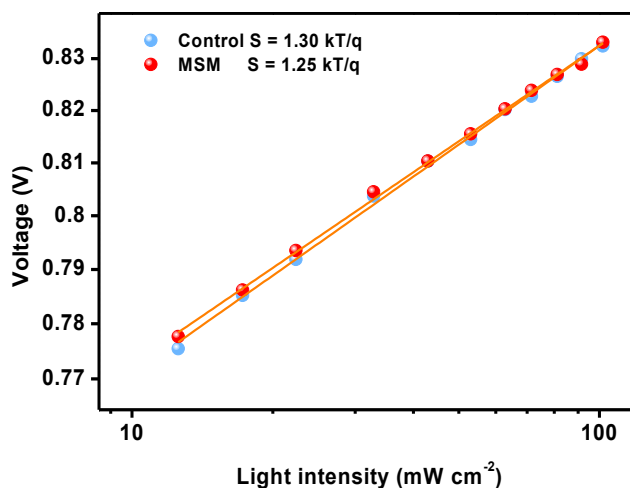
Figure S16. Measured V_{oc} of the control and MSM devices plotted against light intensity on a logarithmic scale, with linear fits to the data (dotted lines). Multiple studies have demonstrated that the light intensity dependence of the V_{oc} can directly provide insight into the role of trap-assisted recombination *versus* 2nd order recombination at the open circuit condition. The V_{oc} and light intensity (I) can be correlated by the following expression $V_{OC} = \frac{E_{gap}}{q} - \frac{kT}{q} \ln[\frac{(1-P)\gamma N_c^2}{PG}]$, where E_{gap} is the energy difference between the HOMO of the electron donor and the LUMO of the electron acceptor, q is the elementary charge, k is the Boltzman constant, T is the temperature in Kelvin, P is the dissociation probability of the electron-hole pairs into free carriers, γ the recombination constant, N_c the density of states in the conduction band, and G the generation rate of electron-hole pairs. This formula contains the dependence of the V_{oc} on the light intensity, as G is the only term directly proportional to the light intensity. Following the rules, the formula predicts a slope $S = (kT/q)$ of the V_{oc} versus the natural logarithm of the incident light intensity. This implies that the slope of V_{oc} versus $\ln(I)$ is equal to kT/q for 2nd order recombination. When trap-assisted recombination is involved, a stronger dependency of V_{oc} on the light intensity is observed, and in this case, the slope of V_{oc} versus $\ln(I)$ is equal to $2\,kT/q$.
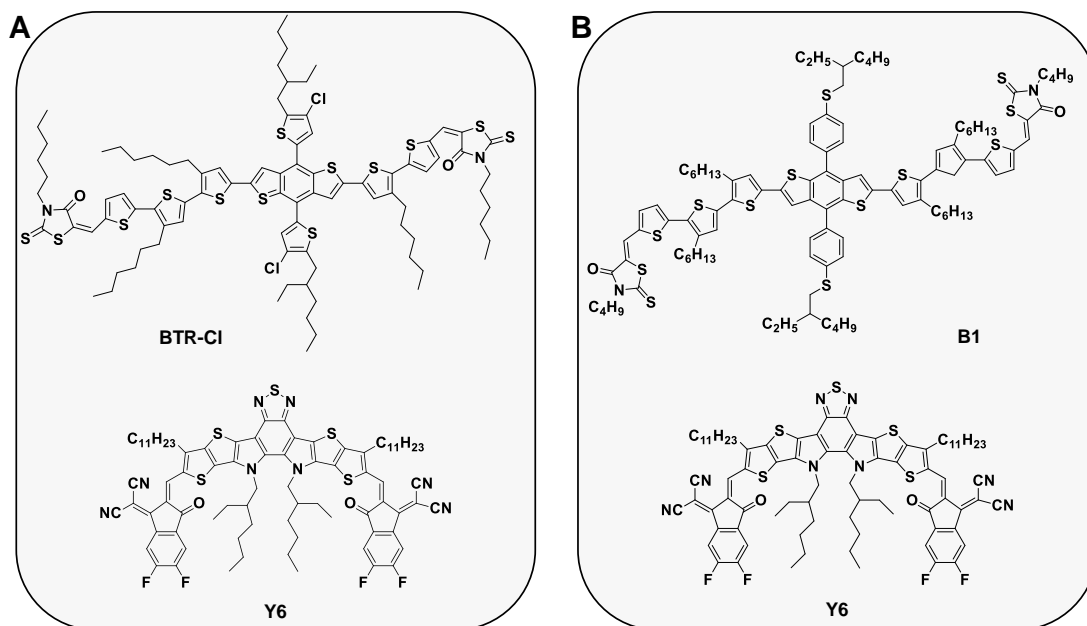
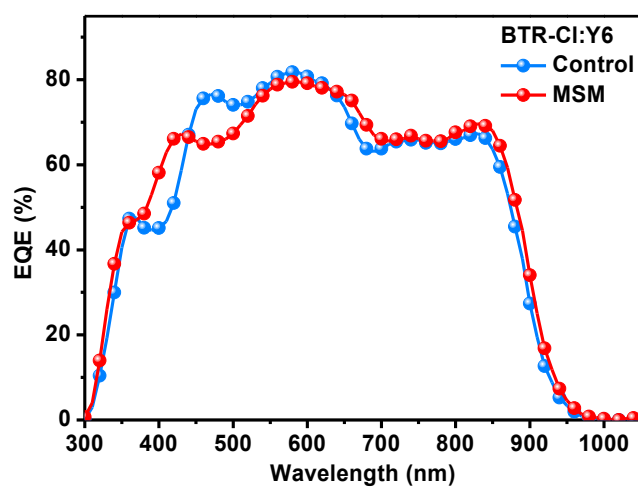Figure S17. Chemical structures of the investigated photovoltaic systems, including (A) BTR-Cl:Y6 system, and (B) B1:Y6 system.

Figure S18. EQE spectra of the control and MSM devices based on BTR-Cl:Y6 photovoltaic system.
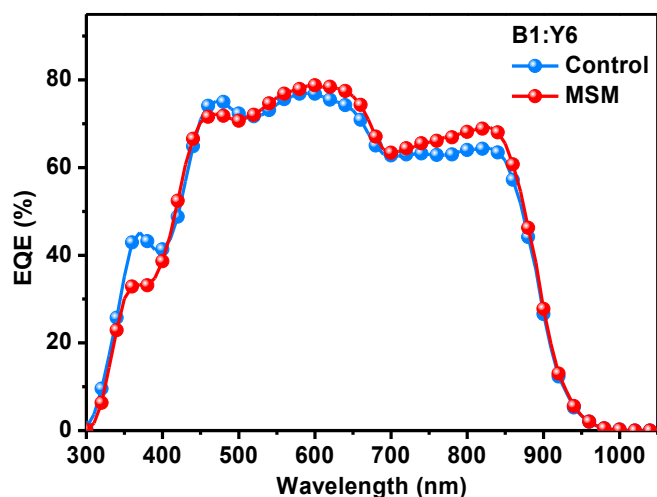
1

2 **Figure S19.** EQE spectra of the control and MSM devices based on B1:Y6 photovoltaic

3 system.

4
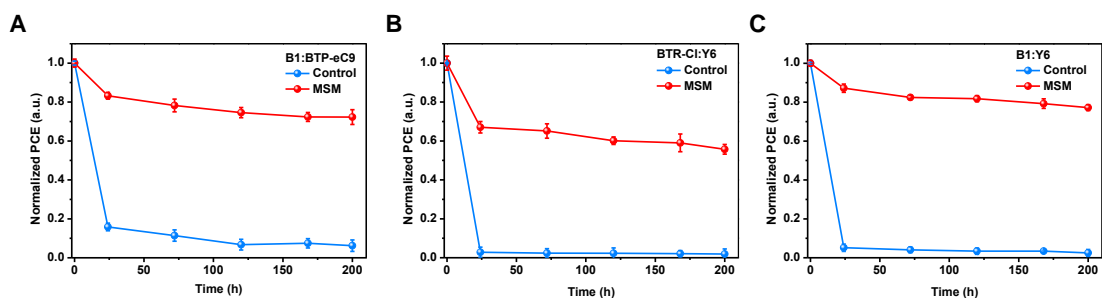
5

6 **Figure S20.** Normalized PCE of the B1:BTP-eC9, BTR-Cl:Y6 and B1:Y6 blend as a

7 function of storing at room temperature in N_2 for 200 hours.

8
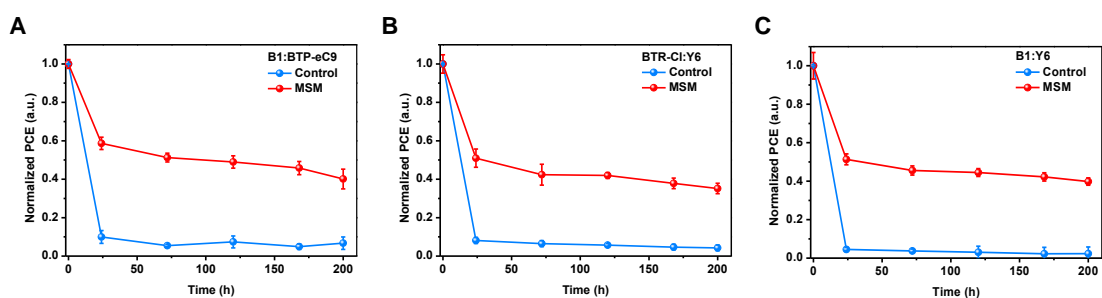
9

10 **Figure S21.** Normalized PCE of the B1:BTP-eC9, BTR-Cl:Y6 and B1:Y6 blend as a

11 function of storing under one sun for 200 hours.

12

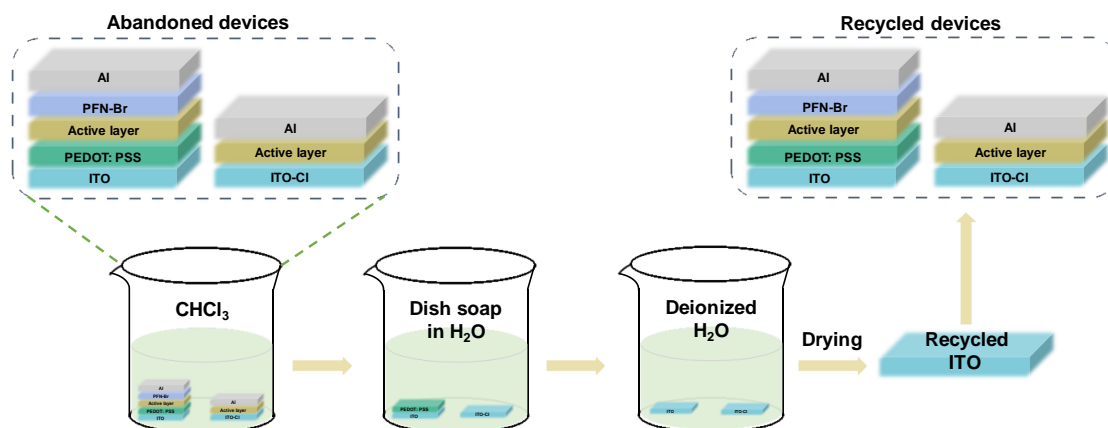**Figure S22.** Device configuration of OSCs and schematic diagram of the recycling processes of ITO from fabricated OSCs. The active layer, interface layers, and the top electrode can be completely cleaned from the ITO substrate by treating in chloroform and dish soap solutions. The cleaning process of the ITO substrate from conventional devices is shown in Figure S21. For a conventional device, ITO was coated by PEDOT:PSS, active layer, PFN-Br, and Al electrode layers, in that order. First, chloroform, which can dissolve the active layer well, was selected to remove the active layer and the top Al electrode and PFN-Br layers. Herein, the conventional devices were placed in chloroform for 15 min. To remove the remaining PEDOT:PSS layer, we placed the samples in a dish soap solution. After the steps above, Al electrode, PFN-Br, PEDOT:PSS, and active layers can be successfully removed from the ITO surface. Finally, the recycled ITO substrate was immersed in deionized water for 15 min. All of the cleaning processes were carried out in the ultrasonic oscillation condition (53 kHz).

1
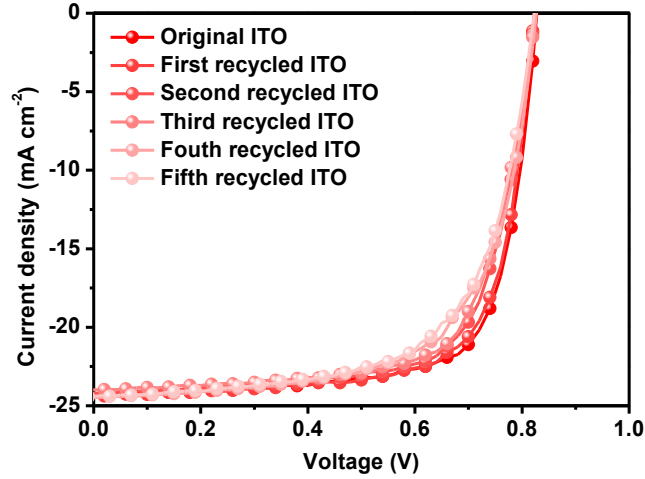
Figure S23. *J-V* curves of the B1:BTP-eC9 solar cells based on original and recycled ITO-Cl electrodes.

Table S5. The photovoltaic parameters of B1:BTP-eC9 solar cells based on original ITO-Cl and recycled ITO-Cl electrodes. The values in parenthesis are the average PCEs obtained from 8 devices.

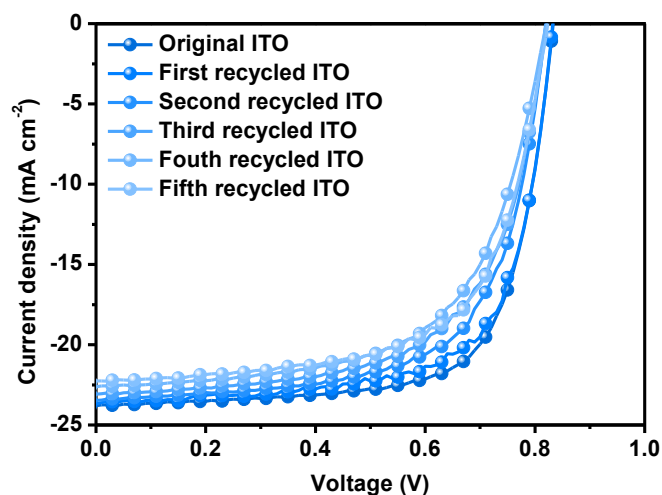| Electrodes	V_{oc} [V]	J_{sc} [mA cm^{-2}]	FF [%]	PCE [%]
Original ITO	0.827	24.30	73.92	14.86 (14.62)
First recycled ITO	0.822	24.38	72.58	14.55 (14.32)
Second recycled ITO	0.824	24.19	70.13	13.98 (13.70)
Third recycled ITO	0.826	24.02	70.11	13.91 (13.64)
Fourth recycled ITO	0.826	24.45	67.52	13.64 (13.38)
Fifth recycled ITO	0.822	24.41	66.18	13.28 (13.00)

7

1

Figure S24. *J-V* curves of the B1:BTP-eC9 solar cells based on original and recycled ITO electrodes.

Table S6. The photovoltaic parameters of B1:BTP-eC9 solar cells based on original ITO and recycled ITO electrodes. The values in parenthesis are the average PCEs obtained from 8 devices.

Electrodes	V_{oc} [V]	J_{sc} [mA cm^{-2}]	FF [%]	PCE [%]
Original ITO	0.833	23.81	70.21	13.92 (13.80)
First recycled ITO	0.832	23.69	69.44	13.69 (13.28)
Second recycled ITO	0.820	23.46	67.72	13.03 (12.66)
Third recycled ITO	0.821	23.08	64.81	12.28 (12.00)
Fourth recycled ITO	0.821	22.61	63.46	11.78 (11.54)
Fifth recycled ITO	0.820	22.24	63.16	11.52 (11.30)

Supplementary Note 1.

Based on the consideration of application scenarios of organic solar cells, nonflexible solar modules are also able to implement commercial applications. Thus, in this work, the techno-economic cost analysis is performed carefully for two types of single solar modules (SSMs) with the control and MSM device architectures (Fig. S24), namely, Control-SSM and MSM-SSM. The cost analysis is considered by assuming an OPV

manufacturing plant located in China. To provide an accurate and realistic estimation, we used some detailed assumptions, as shown in Table S6 and S7, and analyzed the uncertainties of sensitive assumptions. Moreover, considering the device architectures, materials costs in the industrial case as well as standard estimating methodology, we draw on the methods in Ref. 2, and provided the cost projections for the two modules.

The starting point for our cost analysis is the automatic control and production line in solar module manufacture. The costs of photovoltaic materials under the assumption of stable synthesis processes were provided by Solarmer Co. Ltd. Note that the price of active layer materials generally is related to their synthesis complexity. The relevant cost of active layer materials, as well as the upscaled scenarios cost trend estimations based on the data from literature and bulk suppliers, have been made in Tables S8. It indicates that the costs of photovoltaic materials determine the overall material cost of the produced modules. Nevertheless, considering the removal of interfacial layer materials in the MSM-SSMs, the resulting costs of their industrial scenario (19.58 \$/m^2) should be lower than that of the Control-SSMs (21.72 \$/m^2), as provided in Table S9. Furthermore, the direct manufacturing costs (MCs) for the industrial scenarios of the Control-SSM and MSM-SSM are presented in fig. 25A and fig. 25B, respectively. The estimated MCs of these two modules are 26.46 \$ m^{-2} for the Control-SSM and 24.32 \$ m^{-2} for the MSM -SSM, respectively, as shown in fig. S26. In these cost pie charts of current state devices, the materials cost account for 78.56% (Control-SSM) and 77.17% (MSM-SSM) of the overall cost for each module, indicating the costs of materials determine the total material cost of the produced modules. This also highlights the advantage of the two-step solvent treatment strategy for the removal of interfacial layer (IFL) materials in MSM devices. Although the module costs are not significantly dependent on the IFL costs for the industrial scenarios, in the industrial settings many other factors, including reducing the complexity of coating machines, reducing machine maintenance, electricity, and labor costs, *etc*., can also greatly reduce the module costs.

The estimated minimum sustainable price (MSP) values are sensitive to the market

1 price variations of materials and equipment, and capital expenditure innovations. In

2 addition to the reduction of material costs, capital expenditure innovations could drop

3 significantly with reduced capital expenditure. Thus, we further provide the converted

4 MSPs of our investigated two solar modules based on same device efficiencies (10%

5 PCE for the Control-SSM and 10% PCE for the MSM-SSM) and an assumed geometric

6 fill factor (GFF) of 98% which gives the ratio of the active area to the processed area

7 and the irradiance power density at the condition of AM1.5 illumination at 1000 W m^{-2}.

8 The costs of photovoltaics plants are often compared and calculated in \$ Wp^{-1}. The

9 calculation from \$ m^{-2} to \$ Wp^{-1} is done by dividing the costs in \$ m^{-2} by the

10 illumination (AM1.5, 1000 W m^{-2}), and estimated PCE and the GFF value. Under the

11 assumption of a constant module MC, the SSM MSP varies as a function module

12 efficiency from 0.23 to 0.93 \$ Wp^{-1}, and the MSM-SSM MSP changes as a function

13 module efficiency from 0.19 to 0.75 \$ Wp^{-1} (Fig. 4F). Of note is that the highest module

14 efficiency of 20% selected in this work is due to the proper theoretical evaluation. Since

15 this study aims to analyze the techno-economic cost of two solar modules with defined

16 device architectures, we do not wish to compare current MSP values of the relevant

17 technologies as this can be impacted by many other factors (e.g., fully depreciated

18 equipment for production). Despite, it is very important to reduce fabrication materials,

19 optimize device structure, and improve module efficiency for reducing MSP value to

20 gain more competitiveness in the future.

21
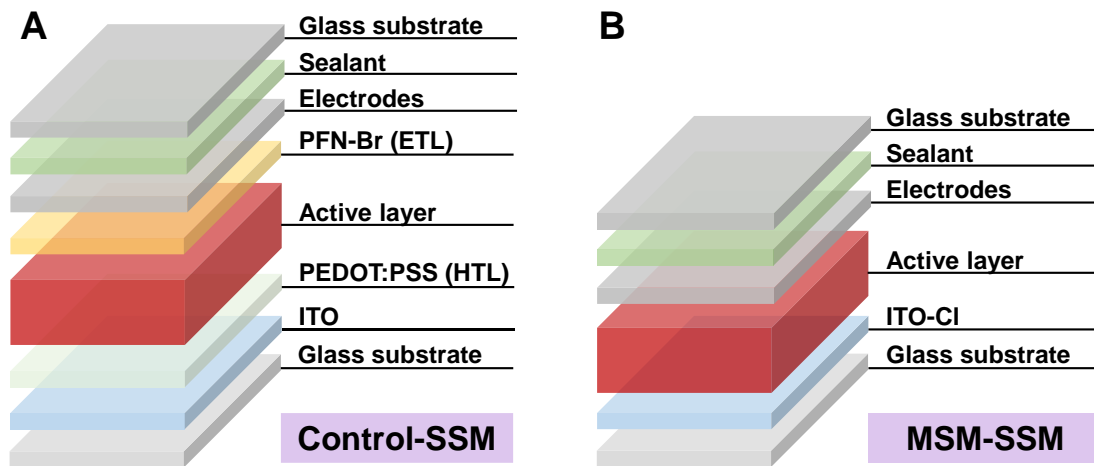
1

2 **Figure S25.** Solar cell layer structures for large scale modules: (A) single solar cell with
3 the control device structure (Control-SSM) and (B) single solar cell with the MSM-type
4 architecture (MSM-SSM) for large-scale device fabrication.

5

6 **Table S7.** Underlying assumptions for organic solar module manufacturing based on
7 the nonflexible organic solar module.

No.	The nonflexible solar module (doctor blade and slot–die techniques)
1	The organic solar module manufacturer is located in Wuhan, Hubei Province, China
2	The module dimension is 1.2 m x 0.6 m (0.72 m^2); the device area of the single cell is 1 cm^2. Thus, the module consists of 3600 cells that are monolithically integrated.
3	The reference module efficiencies of single solar cells are assumed to be 10%.
4	The corresponding nominal power outputs are 72W per panel for the SMM.
5	The total plant operation time is defined as 4200 h/year for each production line.
6	The default deposition throughout is 0.24 min/module for each production line, corresponding to a production rate of 3 m^2/min, resulting in 300 W/min for the corresponding SSMs. The annual production capabilities of each production line are 76 MW/year for the corresponding SSMs.
7	If the production capacity of the manufacturer is ~200 MW/year, the manufacturer needs 3 production lines for the corresponding SSMs.
8	The footprint of 1 production line is estimated to be 400 m^2. The floor space cost is at ~ \$34.88/(m^2·year). After considering the equipment space and offices as well as other functional rooms, we projected that the footprints are 1500 m^2 for a single module manufacturer. The rent of industrial parks is appropriately \$55071/year.
9	To simplify the depreciation of physical properties owned by the manufacturer, we assume the linear depreciation for 20 years.
10	For the sputtering, printing deposition, etc., we assume the material usage efficiency is 80%.

11	Front glass is heat strengthened with anti-reflective coating. Back glass with a thickness of 2.2 mm is used for the encapsulation of nonflexible organic solar modules.
12	Labor cost in Wuhan is appropriately $3.824 per hour for manufacturing work, $7.65 per hour for technical and scientific work. We scale down the labor requirement of 50 manufacturing workers and 25 technical and scientific workers for 200 MW/year production.
13	For utility costs in Wuhan, the average price of electricity to industrial customers is $ 0.146 per kWh; water and sewer rate is $ 0.48/m^3.
14	The maintenance costs for the facilities are set to be 20% of the annual equipment depreciation.
15	SG&A cost is assumed to be 15% of total revenue. Considering the mature manufacturing process, R&D cost is set to zero be as it is expected to be negligible. The average effective tax rate in China at 27% in 2020. The expected internal return for investing 14.4%, which is the average WACC for a China PV manufacturer.

1

2 **Table S8.** Basic assumptions for organic solar module manufacturing based on the
3 corresponding control and MSM SSMs.

Basic assumptions	Control-SSM	MSM-SSM
Module efficiency	10%	10%
Power outputs (per panel)	36 W	36 W
Production rate	300 W/min	300 W/min
Annual production capability	76 MW/year	76 MW/year
Production lines	3	3
Footprints	1500 m^2	1500 m^2
Rent	360,000/year	360,000/year

4

5 **Table S9.** The cost structure of the industrial model of solar modules based on two
6 different device structures.

Layer No.	Material	Supplier	Used account (Unit)	Cost (Unit)	Cost ($/$m^2$)
A	ITO glass	XC Tech.	1 (m^2/m^2)	7.65 ($/$m^2$)	7.65
B	PEDOT:PSS	Heraeus (4083)	1.5 (ml/m^2)	0.61 ($/ml)	0.92
C	B1 donor	Solamer	0.08 (g/m^2)	45.89 ($/g)	3.67
D	BTP-eC9 acceptor	Solamer	0.08 (g/m^2)	38.24 ($/g)	3.06
E	ETLs	Solamer	0.08 (g/m^2)	15.30 ($/g)	1.22
F	solvent	Merck	0.1 (l/m^2)	1.53 ($/l)	0.015

G	Electrode (top)	Dupont	1.2 (g/m^2)	2.29 (\$/g)	2.75
H	Adhesive	DELO	2.5 (g/m^2)	0.31 (\$/g)	0.77
I	glass	XC Tech.	1 (m^2/m^2)	1.53 (\$/m^2)	1.53

Table S10. Two solar module costs for the industrial cost models.

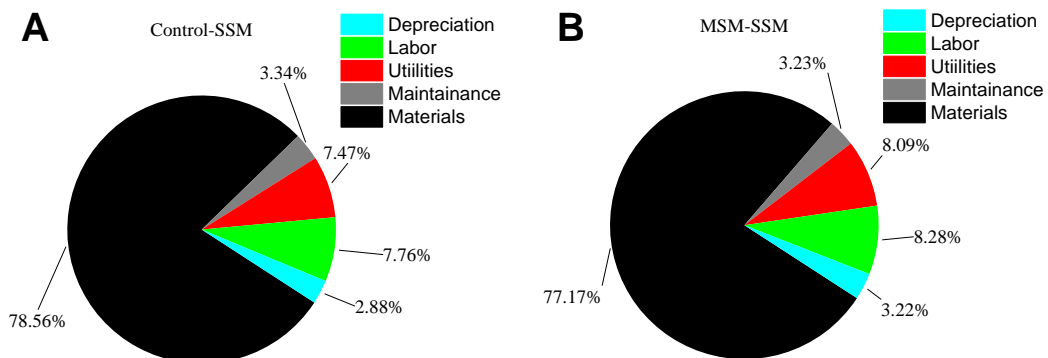| Device Type	Control-SSM	MSM-SSM
Layer structures	A+B+C+D+E+F+G+H+I	A+C+D+F+G+H+I
Industry model cost (\$/m^2)	20.19	18.05
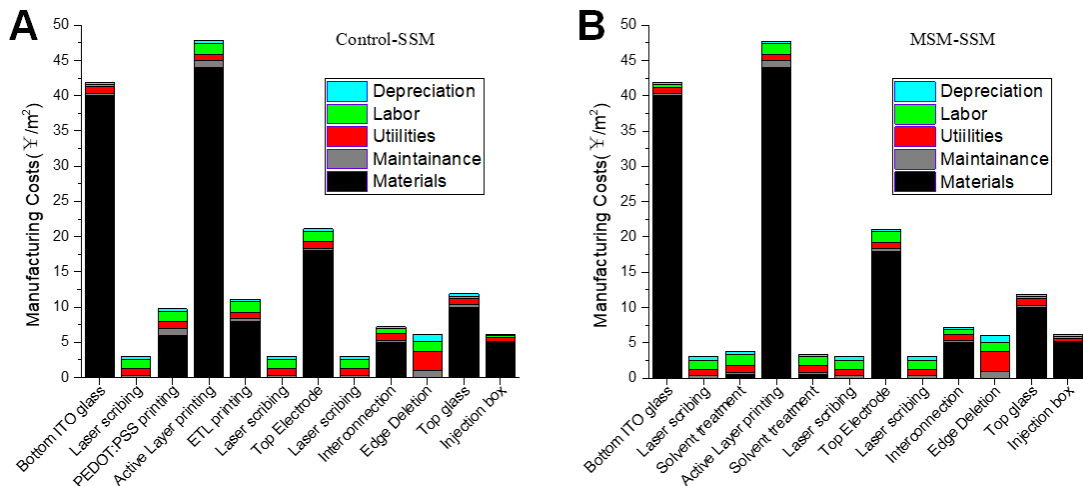
Figure S26. Step-by-step direct manufacturing costs of the (A) Control-SSM and (B) MSM-SSM.

Figure S27. Materials cost breakdown of the (A) Control solar module with a total manufacturing cost of 26.46 \$ m^{-2} and (B) MSM-type solar module with a total manufacturing cost of 24.32 \$ m^{-2}.

Supplemental References

1.   Y. Hu, P. Wei and X. Wang, *Phys. Rev. Applied*, 2018, **10**, 054024,.

2.   J. Guo and J. Min, *Adv. Energy Mater.* 2019, **9**, 1802521.